Martensitic Transformation and Crystalline Structure of $Ni_{50}Mn_{50-x}Sn_x$ Melt-Spun Heusler Alloys

Rim Ameur [1,2]**, Mahmoud Chemingui** [1]**, Tarek Bachaga** [1,2][ID]**, Lluisa Escoda** [2]**,
Mohamed Khitouni** [1][ID] **and Joan-Josep Suñol** [2,*][ID]

[1] Laboratory of Inorganic Chemistry, UR 11ES73, Université de Sfax, Soukra Road km 3,5, BP 1171, 3018 Safx, Tunisia; rim.ameur@yahoo.fr (R.A.); mahmoud.chemingui@fss.usf.tn (M.C.); bachagatarak@yahoo.fr (T.B.); khitouni@yahoo.fr (M.K.)

[2] Department of Physics, Universitat de Girona, Campus Montilivi s/n, 17003 Girona, Spain; lluisa.escoda@udg.edu

* Correspondence: joanjosep.sunyol@udg.edu

check for updates

Abstract: The structure and thermal behavior are key factors that influence the functional response of Ni–Mn–Sn alloys. The present study reports the production as well as the structure and thermal analysis of melt-spun (solidification rate: 40 ms^{-1}) Ni_{50} $Mn_{50-x}Sn_x$ (x = 10, 11, 12 and 13 at.%) alloys. X-ray diffraction measurements were performed at room temperature. The austenite state has an $L2_1$ structure, whereas the structure of the martensite is 7M or 10M (depending on the Sn/Mn percentage). Furthermore, the structural martensitic transformation was detected by differential scanning calorimetry (DSC). As expected, upon increasing the Sn content, the characteristic temperatures also increase. The same tendency is detected in the thermodynamic parameters (entropy and enthalpy). The e/a control allows the development production of alloys with a transformation close to room temperature.

Keywords: Heusler alloys; martensitic transformation; DSC; XRD; rapid solidification

1. Introduction

The main characteristic of the shape memory alloys (SMA) is the existence of a martensitic transformation. This transformation is shear-dominant, diffusion-less, and it is related to the nucleation and growth of the martensitic phase from a high ordered austenitic phase. This phenomenon is found by cooling from the parent austenite phase. The crystallographic structure of the martensite can be tetragonal, orthorhombic, or monoclinic. The SMA alloys with ferromagnetic behavior (ferromagnetic shape memory alloys, FSMA) combine (a) the shape memory effect and (b) the ferromagnetic response. $Ni_{50}Mn_{25+x}Z_{25-x}$, (Z = Ga, In, Sn, Sb) Heusler alloys are examples of FSMA with interesting functional properties: (a) large magnetic field induced strain [1], (b) giant magnetocaloric effect [2], and (c) giant magnetoresistance [3]. Likewise, calorimetry is useful to determine structural solid-state transformation temperatures of ferromagnetic alloys [4–8]. The transformation temperatures of SMAs strongly depend on the composition. Accordingly, their values are spread in a wide range [9]. For these, the accurate selection of the composition facilitates that the temperature range of the transformation becomes in the desired range for specific devices and sensors. Likewise, calorimetry checks the occurrence of the transformation, because sometimes the structural transformation is inhibited.

The Heusler crystallographic structure is the highly ordered $L2_1$ cubic crystal structure. In this type of alloy, off-stoichiometric Heusler $Ni_{50}Mn_{50-y}X_y$ (X = In, Sn, Sb) alloys have been identified as potential candidates for functional applications in sensors, actuators, and magnetic refrigeration. Heusler $Ni_{50}Mn_{50-x}Sn_x$ alloys production with 10 < x < 16.5 was first reported by Sutou et al. [10]. Likewise, $Ni_{50}Mn_{50-y}Sn_y$ (y = 5–25 at.%) alloys have been previously investigated by Krenke et al. [11].

The austenite was observed to be L2$_1$, while the martensitic structure depends on the composition. Complementary works were performed by Brown et al. [12] and Koyama et al. [13], by reporting on their magnetoelasticity. Therefore, the Ni–Mn–Sn system is one of the most promising Heusler FSMA.

In our present work, we have chosen four alloys in the Ni–Mn–Sn system to be produced and analyzed (by modifying the Sn–Mn content). Specifically, we chose Ni$_{50}$Mn$_{50-x}$Sn$_x$ (x = 10, 11, 12 and 13 at.%) melt-spun ribbons to develop materials with a martensitic transformation temperature ranging above, near, or below room temperature. This work focuses on the crystallographic structure and on the calorimetric characterization. The ribbon shape allows the development of samples with a higher surface/volume ratio than bulk alloys, favoring the heat transfer if these samples are introduced in specific devices for applications such as magnetic refrigeration. These alloys can be integrated in magnetic cooling devices as an alternative to conventional refrigeration systems, usually working near room temperature. The alloys can be also used to develop magnetic sensors or magnetic actuators.

2. Materials and Methods

As-cast ingots with elemental composition Ni$_{50}$Mn$_{50-x}$Sn$_x$ (x = 10, 11, 12 and 13) (labeled as Sn10, Sn11, Sn12, and Sn13, respectively) were produced by conventional argon arc melting (elements purity: 99.98% Ni, 99.98% Mn, and 99.99% Sn, in an arc-melting device (Bühler MAM-1, Bodelshausen, Germany). The samples were melted four times to ensure a good initial homogeneity. The produced bulk samples were melted by induction (quartz crucibles with a circular nozzle of 0.6 mm) and then ejected (by applying an overpressure) onto a copper wheel (surface linear speed: 40 ms^{-1}). Finally, they are annealed at 600 K for 1 h favoring the homogeneity. The arc melting, melt spinning, and annealing processes were carried out in an argon environment. The details of characterization and the results of various experimental measurements in this work are obtained by several techniques.

The microstructure, morphology, and composition of ribbons was determined through Scanning Electron Microscopy (SEM) in a ZEISS DSM-960A (Oberkochen, Germany) microscope coupled with EDS microanalysis. X-ray diffraction (XRD, Bruker, Karlsruhe, Germany) patterns were collected at room temperature in a Siemens D500 X-ray powder diffractometer (Cu-K$_\alpha$ radiation). The structure of samples was refined by applying the Rietveld refinement method using Jana software (Jana 2006, Jana. Praha, Czech Republic) [14]. The thermal analyses (first cycle) were carried by means of differential scanning calorimetry (DSC) at a heating/cooling rate of 10 K/min under argon atmosphere. DSC investigations above room temperature were performed by heating/cooling in the Setaram Setsys DSC system, and the DSC scans below room temperature were performed by cooling/heating in the Mettler-Toledo DSC 30 (liquid nitrogen refrigeration, dewar flask, Columbus, Ohio, USA).

3. Results and Discussion

The experimental results of the XRD, DSC, and SEM measurements of Ni$_{50}$Mn$_{50-x}$Sn$_x$ (x = 10, 11, 12 and 13) ribbons are discussed in this paper. To begin with, the martensitic or austenitic structures have been determined by X-ray diffraction. The crystal structure at room temperature is always essential to decide the thermal analysis procedure [15]. If the phase detected by XRD is cubic, then the martensitic transition (if it occurs) must be found below room temperature. However, if the detected phase is less ordered, then the inverse austenitic transformation (if it occurs) must be found by heating the sample. Figure 1 shows the room temperature XRD patterns of the samples labeled as Sn10, Sn11, and Sn12. The reflection peaks are identified to correspond to a monoclinic structure with modulation. Its structural parameters are given in Table 1. Thus, the relative peak intensities are different. The monoclinic phase is the same, 7M, in Sn10 as in Sn11 alloys. However, it is 10M in Sn12. It is known that the Heusler alloys may have anisotropy, texture, and/or modulation effects [16]. In contrast, Figure 2 gives the XRD pattern of the sample labeled as Sn13. It shows also a unique phase—in this case, an austenitic cubic phase. The detection and identification of the (111) and (311) reflection peaks confirm that the highly ordered L2$_1$ structure is obtained. The lattice parameter is a = 0.59827(5) nm (space group: Fm-3m). However, the alloy Sn13 is in the austenite phase.
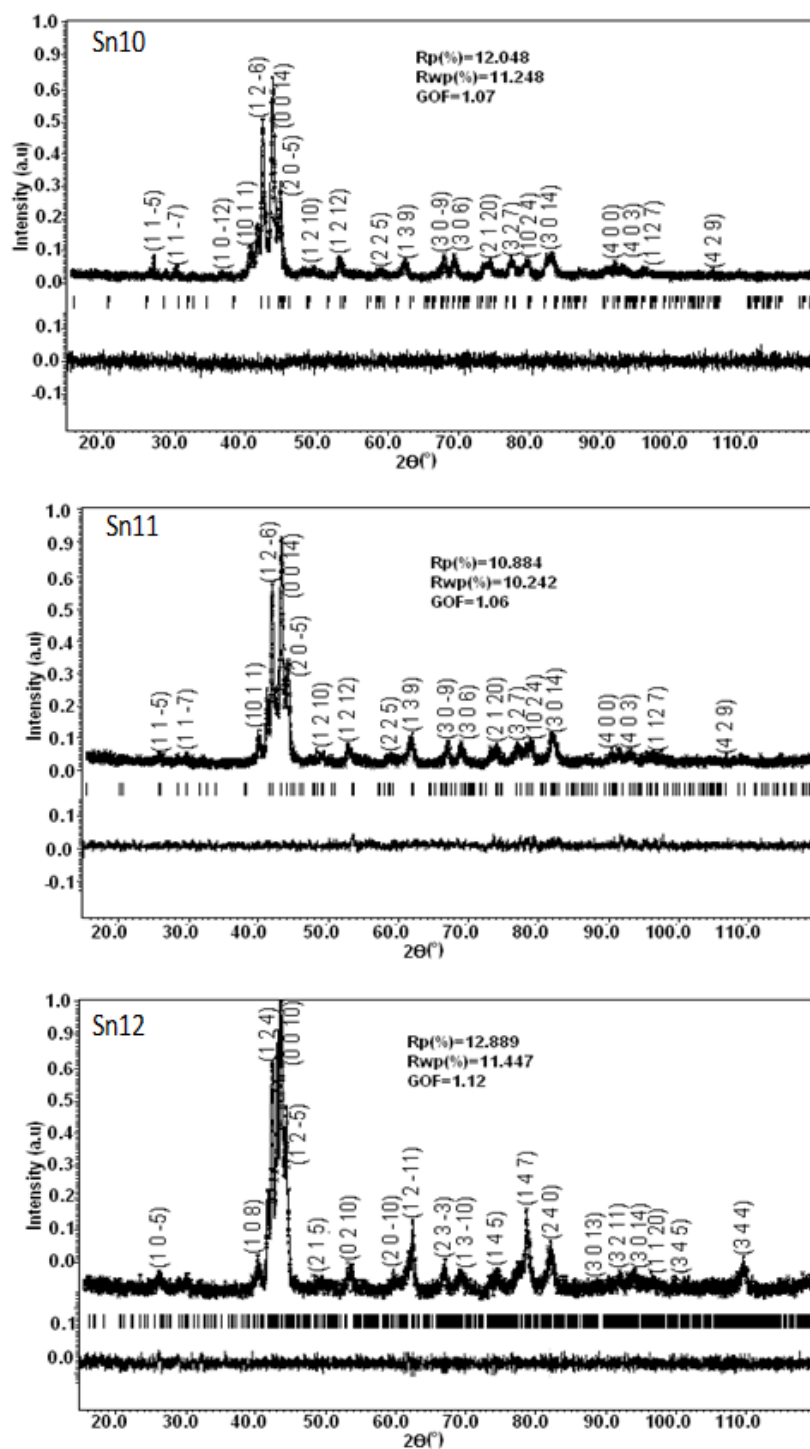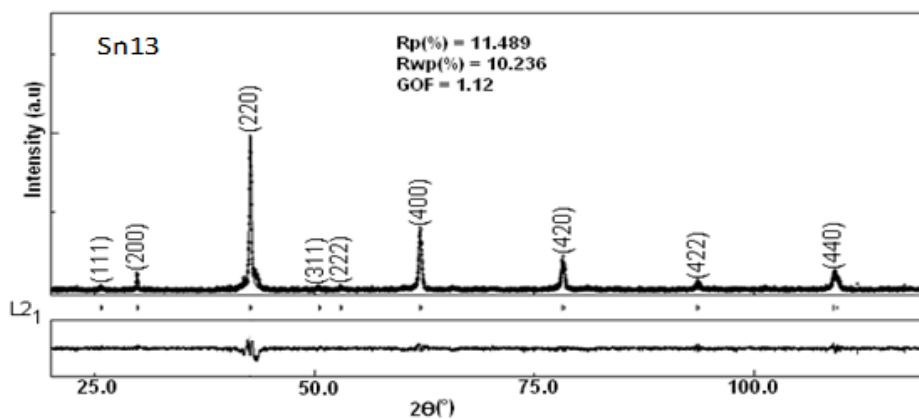
Figure 1. X-ray diffraction patterns (room temperature) for samples labeled as Sn10, Sn11, and Sn12. The crystallographic structure is identified as monoclinic 7M for Sn10 and Sn11 and 10M for Sn12.

Table 1. Crystallographic parameters of samples labeled as Sn10, Sn11, Sn12, and Sn13.

Alloy/Sample	Crystallographic Structure	Lattice Parameters/nm
Sn10	Monoclinic 7M	$a = 0.42824(4)$ $b = 0.57874(7)$ $c = 0.43426(5)$ $\beta = 93.86°$
Sn11	Monoclinic 7M	$a = 0.42806(6)$ $b = 0.57277(3)$ $c = 0.43321(8)$ $\beta = 93.84°$
Sn12	Monoclinic 10M	$a = 0.43326(2)$ $b = 0.56412(9)$ $c = 2.11706(7)$ $\beta = 88.32°$
Sn13	Cubic L2$_1$	$a = 0.59827(5)$

Figure 2. X-ray diffraction pattern (room temperature) for $Ni_{50}Mn_{37}Sn_{13}$ alloy. The crystallographic structure is identified as cubic L2$_1$.

In the following, the lattice constants calculated in this work are coherent with those found in the literature [11,15]. It is obvious that the microstructure is sensitive to composition. Thus, the formation of different phases is plausible. It should be remarked that while substituting the Mn element by Sn, the transition is displaced to higher temperatures, and the crystal structure (room temperature) of the alloys evolves from the austenitic structure with high symmetry from a martensitic structure with low symmetry.

The small variation of the lattice parameters in Sn10 and Sn11 alloys is explained by the different atomic radius of Mn and Sn. Rapid cooling can induce the retention of the austenite, but in our work, austenite was not detected in XRD patterns of alloys with a modulated structure. Furthermore, rapid cooling can also lead the suppression of the ordered phase. This effect has not been detected. Concretely, the austenite has the L2$_1$ structure, not the less ordered B2 structure.

The typical SEM micrographs corresponding to the wheel surface, free surface, and cross-section of alloys labeled as Sn10, Sn11, Sn12, and Sn13 are presented in Figure 3. Micrographs 3a1, 3a2, 3a3, and 3a4 are obtained in the wheel surface. The micrographs of the Sn10 (a1), Sn11 (a2), and Sn12 (a3) ribbons have the martensitic microstructure (lamellar). On the other hand, the micrograph of the Sn13 (a$_4$) ribbon shows a granular microstructure (Figure 3a4) typical of austenitic grains. These ribbons are obtained as flakes because they are obtained at a high solidification rate (10^6 K s^{-1}) and are also fragile and brittle. The micrographs (free surface) of alloys Sn10, Sn11, Sn12, and Sn13 are shown in Figure 3b1–b4, respectively These flakes have a coarse granular microstructure (average grain size value around 1–2 μm); the average grain size values are well below those obtained in bulk alloys (10 to

20 μm) [17]. The micrographs (cross-sections normal to ribbon plane) for Sn10, Sn11, Sn12, and Sn13 alloys can be observed respectively in Figure 3c1–c4. It shows a collinear granular columnar-type microstructure (Figure 3c1–c4). The columnar grains are likened to fast crystallization and growth kinetics (perpendicular to the wheel surface). Furthermore, equiaxed grains were found as a fine layer close to the wheel surface. The Sn10, Sn11, Sn12, and Sn13 ribbon thickness averages are about 11, 16, 10, and 9 μm. The EDS composition results are $Ni_{50.3}Mn_{39.5}Sn_{10.2}$, $Ni_{50.5}Mn_{38.4}Sn_{11.1}$, $Ni_{50.1}Mn_{37.6}Sn_{12.3}$, and $Ni_{50.6}Mn_{36.3}Sn_{13.1}$ for alloys Sn10, Sn11, Sn12, and Sn3, respectively. Thus, EDS microanalysis does not show a significant shift on compositions.
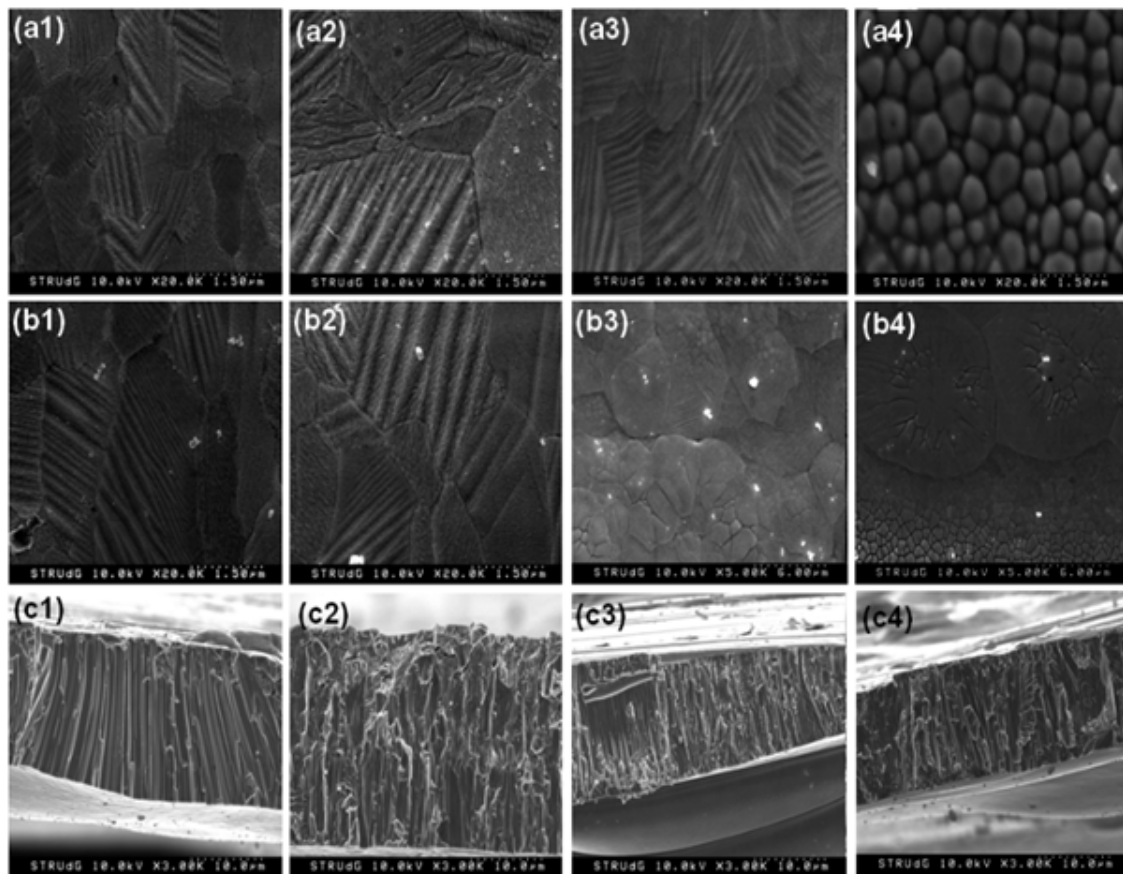

Figure 3. Typical SEM micrographs of the different regions: (**a1**–**a4**). Wheel surfaces, (**b1**–**b4**). Free surfaces and (**c1**–**c4**). Fractured cross-sections of samples labeled Sn10, Sn11, Sn12, and Sn13, respectively.

From XRD diffraction patterns analysis, it is clear that if the martensitic transformation is present in the alloy, the DSC scans of Sn10, Sn11, and Sn12 ribbons should be performed by a heating/cooling cycle from room temperature. Likewise, the DSC scan of alloy Sn13 should be performed by a cooling/heating cycle, also from room temperature. As shown in Figure 4, the DSC scans show a well-defined peak (the exception is alloy Sn13 on heating showing small humps, which were probably due to a local inhomogeneous composition). Rekik et al. [18] and Zeng et al. [19] have found similar results. In fact, DSC curves allow all the characteristic first-order transformation temperatures: austenite to austenite (on cooling) start and finish (M_s and M_f), and the reversible martensite to austenite (on heating) start and finish (A_s and A_f). Values are given in Table 2. The beginning and the end of the transformation of the temperatures have been determined by the procedure described in ref. [18]. Likewise, it is known that the characteristic temperatures have been reported to depend on outer electron concentration [20]. Another thermal parameter is the width of the hysteresis, ΔT ($\Delta T = As - M_f$). In this work, the values of this parameter range between 5 and 13 K. Furthermore, the thermal hysteresis range is increased

upon increasing the elastic and surface energies [15]. Consequently, the nucleation of the martensitic phase implies super cooling.
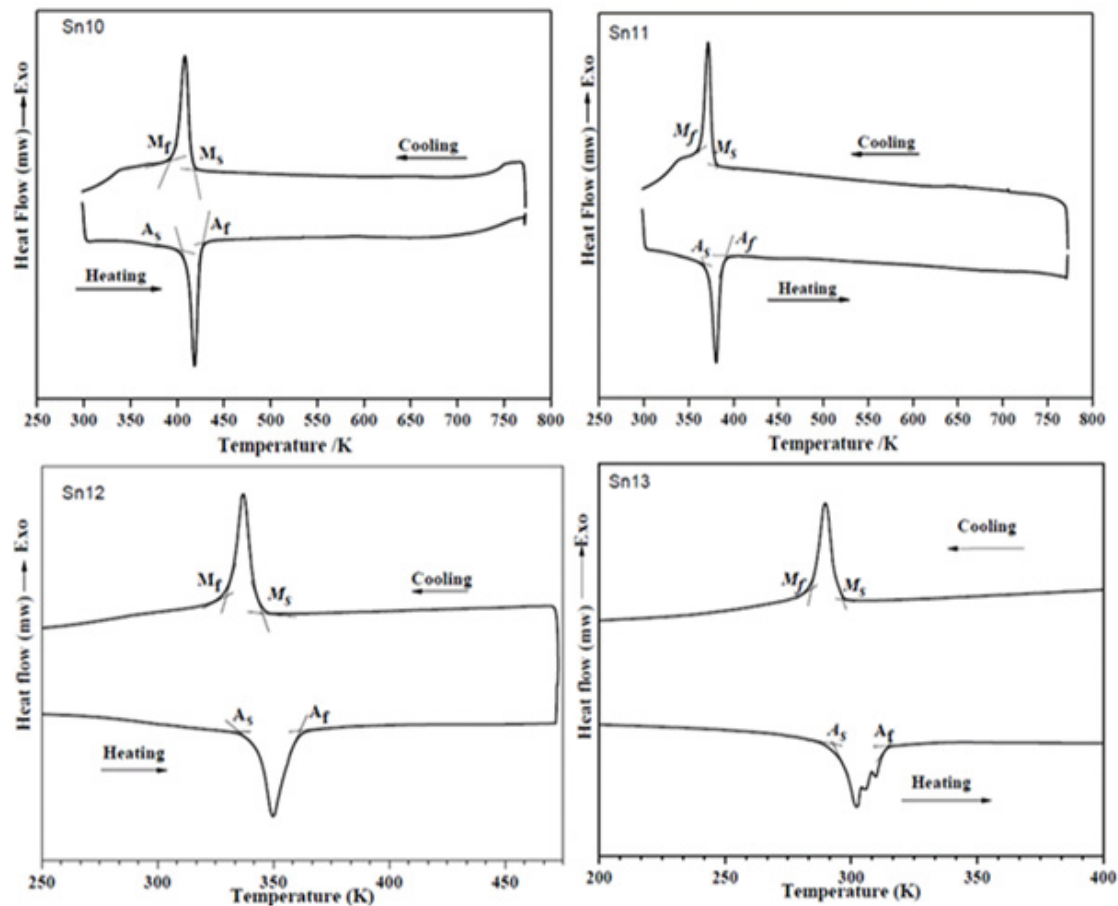

Figure 4. Differential scanning calorimetry (DSC) cyclic scans for samples labeled Sn10, Sn11, Sn12, and Sn13 at a heating/cooling rate of 10 K/min. Arrows indicate heating (up: austenite to martensite) and cooling (down: martensite to austenite).

Table 2. Characteristic structural and hysteretic temperatures (±1 K): (h) and (c) indicate calculated on heating or cooling, respectively.

Sample	e/a	M_s/K	M_f/K	A_s/K	A_f/K	T_0/K	ΔH/J mol^{-1}	ΔS/J mol^{-1} K^{-1}
Sn10	8.20	418.5	392	405	427	422.75	1326 (h) 1334 (c)	3.134 (h) 3.156 (c)
Sn11	8.17	380	361	367	391	385.5	1112 (h) 1126 (c)	2.855 (h) 2.921 (c)
Sn12	8.14	345	330	335	361	353.2	890 (h) 894 (c)	2. 512 (h) 2.531 (c)
Sn13	8.11	297	284	293	315	306	669 (h) 665 (c)	2.186 (h) 2.173 (c)

In addition, the equilibrium temperature T_0 (the temperature at which the extrapolated Gibbs energies of martensitic and austenitic phases are equal) gives additional information about the shift of the structural transformation. It is obtained from the expression $T_0 = 1/2(M_s + A_f)$ [20]. The calculated T_0 values are about 422.75, 385.5, 353.25, and 306 K for the Sn10, Sn11, Sn12, and Sn13 ribbons, respectively. It should be remarked that all characteristic temperatures decrease upon increasing/decreasing the Sn/Mn content.

The transformation temperatures of shape-memory alloys strongly depend on chemical composition. It has been also previously reported for other Ni–Mn–(In,Sn) Heusler alloys [21,22] that temperatures are spread over a wide range. Another relation is found with the average number of valence/outer electrons by atom (e/a). The theoretical values of e/a are calculated: 8.20, 8.17, 8.14,

and 8.11 for samples with 10, 11, 12, and 13 at. % Sn, respectively. In further analysis, we use the e/a values calculated from EDS microanalysis: 8.203, 8.182, 8.134 and 8.125 (close to theoretical parameters) for Sn10, Sn11, Sn12, and Sn13 respectively. There are several pathways to modify the structural transition temperatures in Heusler alloys: controlled addition, the modification of elemental ratio contents, annealing [23]. Sanchez-Alarcos et al. [24] have reported the structural temperatures as dependent on e/a. In the literature, it has been found that sometimes, there is a linear correlation between e/a and the temperatures. For the phase diagrams, the martensitic start temperature was selected [25]. We note that all the measured/calculated temperatures decrease with the increase of Sn content as well as with the decrease of e/a. The current result is coherent with Coll et al. [15], Rekik et al. [18] and other Ni–Mn–Z (Z = Ga, Sn, In, and Sb) alloys [26].
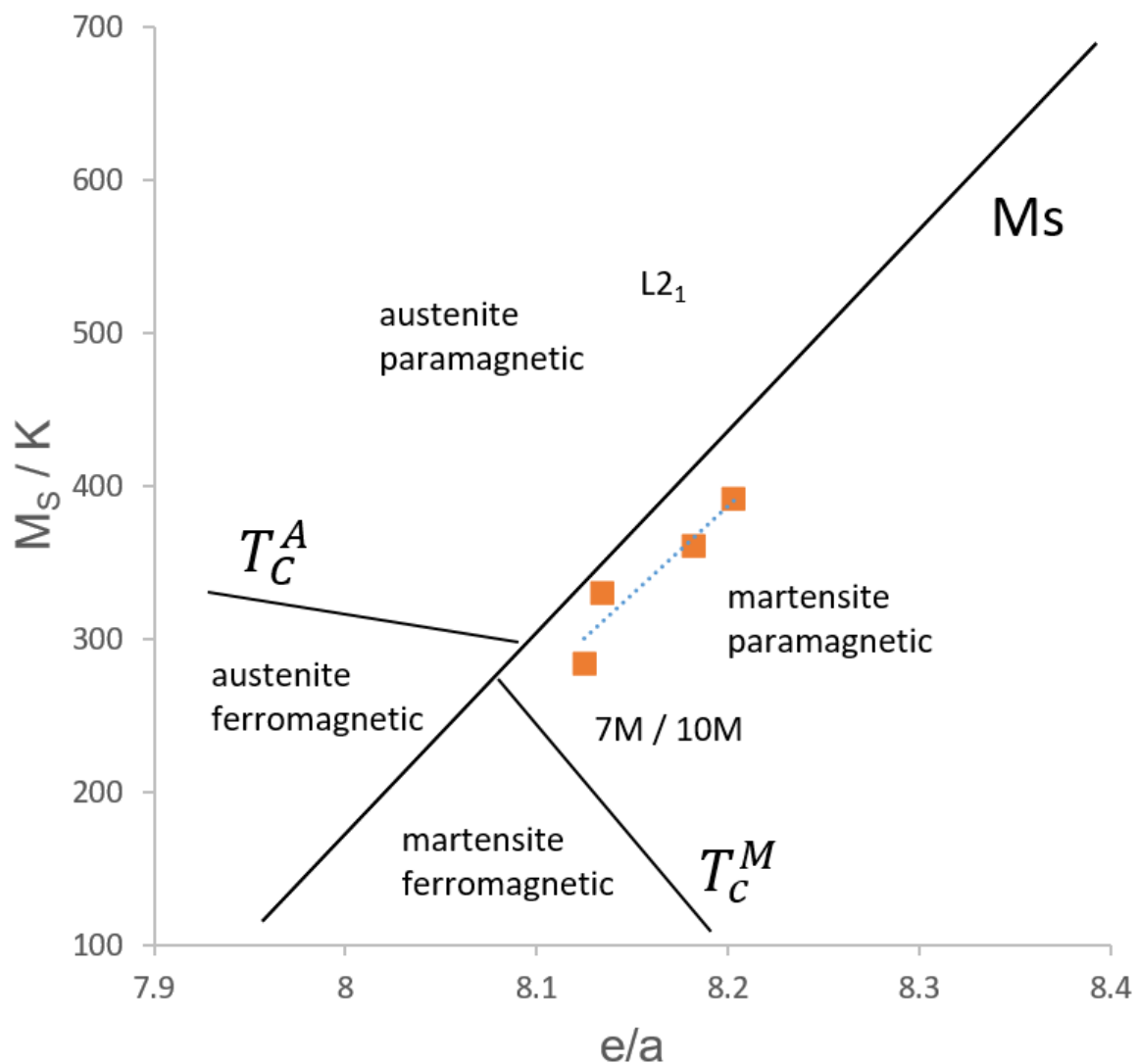

Figure 5. Phase diagram (martensite start versus e/a). Adapted from reference [27] (squares this work).

Thus, by compositional (and e/a) accurate selection, it is possible to design an alloy with a desired working temperature range. Nevertheless, the functional properties (magnetocaloric effect, magnetoresistance, exchange bias, magnetic field-induced strain) do not depend only on e/a. There are other parameters linked to functional response: magnetic interactions between atoms, the concurrence of the structural and Curie ferromagnetic transformation, and so on. Likewise, characteristic temperatures also depend on the production techniques, processing conditions, and ulterior annealing. For it, different temperatures values and ranges can be found in the literature for alloys with composition

close to those of this study [28]. In references [22,29], the temperatures are lower/higher for Sn13 and Sn10 alloys, respectively. It is known that the shape, geometry, and processing parameter (as the wheel speed) influence the characteristic temperatures [17,30]. For it, it is recommended to compare alloys produced at the same conditions or to be careful in the comparative analysis. Figure 5 shows a phase diagram of the martensite start temperature versus e/a. The comparison is performed with data obtained in bulk alloys [27]. Our values are lower due to the lower dimensionality of the samples. Nevertheless, the linear trend corroborates the option to produce alloys with the thermal hysteresis interval at the desired temperature range. Likewise, the crystallographic phases detected at room temperature are in good agreement with those expected.

The enthalpy and entropy structural changes (ΔH and ΔS, respectively) are calculated from calorimetry data [11]. The calculated values for structural ΔH and ΔS are shown in Table 2. The linear tendency of both parameters as a function of e/a is confirmed by linear fitting (Figures 6 and 7), where the values are the average of cooling (c) and heating (h) of Table 2.
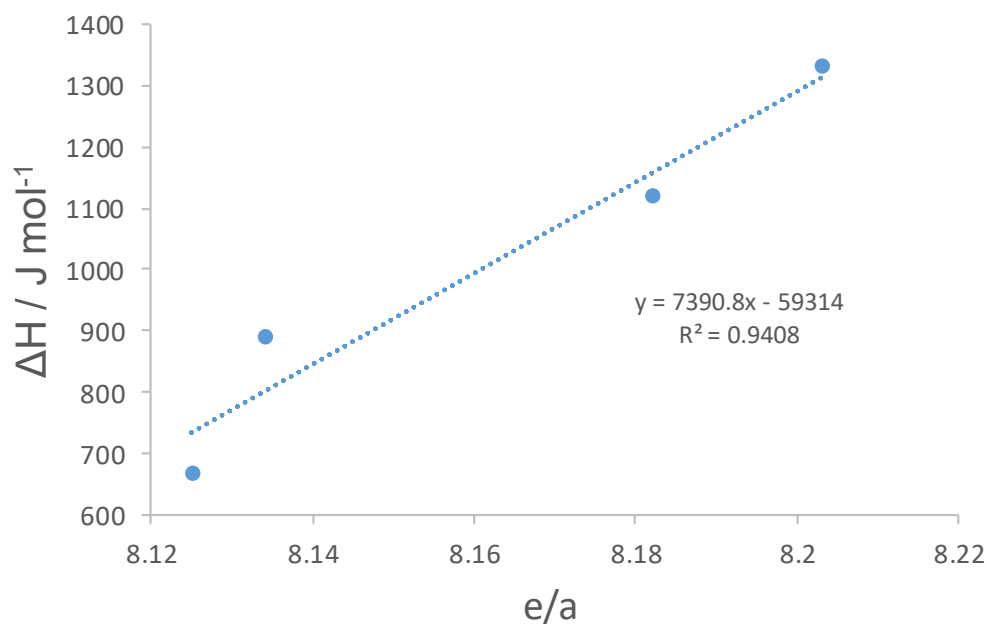

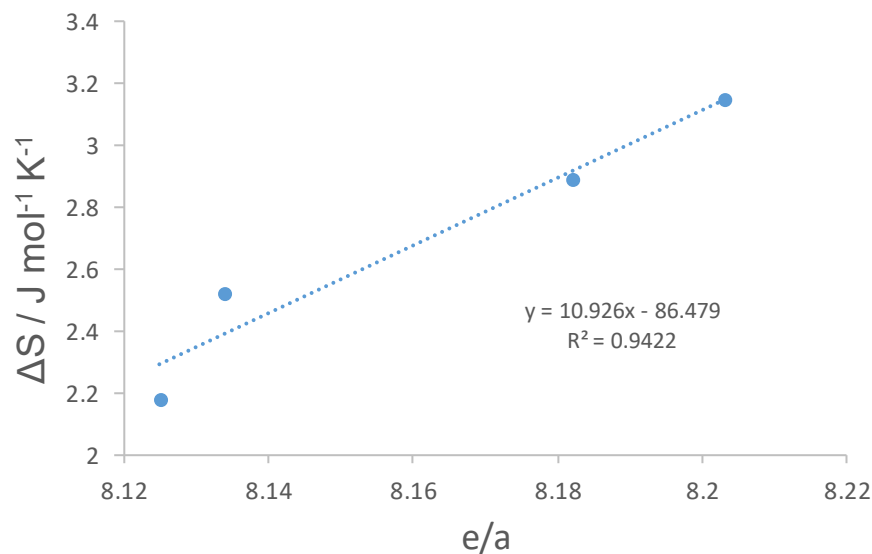**Figure 6.** Enthalpy of the structural transformation versus e/a.

Figure 7. Entropy of the structural transformation versus average number of valence/outer electrons by atom (e/a).

It is noted that the thermodynamic parameters (enthalpy and enthalpy) decrease with the increase/decrease of the Sn/Mn content. This phenomenon is also linked to a decrease in e/a (in Figures 5–7, the e/a values obtained from EDS were used). The same trend (with e/a) was found by Krenke et al. [11] in Ni–Mn–In and Ni–Mn–Sn; specific reported values are $\Delta H = 1642$ J mol^{-1} and $\Delta S = 3.7$ J mol^{-1} K^{-1} for Sn10 and e/a = 8.292. Nevertheless, in the Ni–Mn–In system [11], significant e/a dependence was not found. In our work, a linear fitting dependence was detected (fitting parameters are given inside Figures 6 and 7). Additional compositions obtained at the same processing conditions are needed to check if this linear dependence is extended along the Sn composition; it is probable that as the composition range increases, this behavior disappears.

Complementary studies on the magnetic and magnetocaloric response of these alloys should be performed to check their potential applicability.

4. Conclusions

To conclude, the most important findings on the structures and martensitic transformation parameters of the Ni$_{50}$Mn$_{50-x}$Sn$_x$ (x = 10, 11, 12, and 13) ribbons are in this work are as follows:

(i)   From XRD Rietveld analysis: alloys with Sn10 and Sn11 have a textured monoclinic 7M martensite structure, while those with Sn12 have a 10M martensite structure. In contrast, the alloy with Sn13 has an austenite cubic L2$_1$ structure.

(ii) The results from calorimetric measurements confirmed that all samples present a reversible transition (the austenite to martensite), and the change of the composition has an obvious effect on transformation behavior. With the increase/decrease of Sn/Mn content, the characteristic transformation temperatures (As, Af, Ms, Mf) drop to low temperature, which is due to the decrease of e/a. Consequently, Ms increases as the e/a parameter increases. In addition, the e/a control permits the development of alloys with the desired transformation temperatures. Likewise, the entropy and enthalpy change related to the transformation decreases as the e/a decreases. These trends cannot be extrapolated to further studies on functional response.

(iii) Morphological analysis indicated that the SEM observations exhibit a microstructure with columnar grains and preferential orientation.

Conflicts of Interest: The authors declare no conflict of interest.

References

1. Li, Z.-H.; Li, Z.; Yang, J.; Li, D.; Yang, B.; Zhang, Y.; Esling, C.; Zhao, X.; Zuo, L. Large magnetic entropy change and magnetostrain in a directionally solidified Ni$_{45.7}$Co$_{4.2}$Mn$_{37.3}$Sb$_{12.8}$ alloy. *J. Magn. Magn. Mater.* **2020**, *500*, 166379. [CrossRef]

2. Sokolovskiy, V.; Miroshkina, M.; Zagrebin, M.; Buchelnikov, V. Prediction of giant magnetocaloric effect in Ni$_{40}$Co$_{10}$Mn$_{26}$Al$_{14}$ Heusler alloys: An insight from ab initio and Monte Carlo calculations. *J. Appl. Phys.* **2020**, *127*, 163901. [CrossRef]

3. El-Khabib, S.; Batti, K.P.; Srivastava, V.; James, R.D.; Leighton, C. Nanoscale magnetic phase competition throughout the Ni$_{50-x}$Co$_x$Mn$_{40}$Sn$_{10}$ phase diagram: Insights from small-angle neutron scattering. *Phys. Rev. Mater.* **2019**, *3*, 104413. [CrossRef]

4. Bouabdallah, M.; Cizeron, G. Differential scanning calorimetry of transformation sequences during slow heating of Cu–Al–Ni shape memory alloys. *J. Therm. Anal. Calorim.* **2002**, *68*, 951–956. [CrossRef]

5. Auguet, C.; Isalgué, A.; Lovey, F.C.; Pelegrina, J.L.; Ruiz, S.; Torra, V. Metastable effects on martensitic transformation in SMA. *J. Therm. Anal. Calorim.* **2007**, *89*, 537–542. [CrossRef]

6.   Topel-Zeren, E.; Aksit, A.; Aydogdu, Y. Shape memory effect of polymeric composite materials filled with NiMnSbB shape memory alloy for textile materials. *Mater. Res. Express* **2020**, *7*, 055702. [CrossRef]

7.   Canbay, C.A.; Karaduman, O.; Özkul, I. Lagging temperatura problema in DTA/DSC measurement on investigation of NiTi SMA. *J. Mater. Sci. Mater. Electron.* **2020**. [CrossRef]

8.   González, A.; Bonastre, J.; Escoda, L.; Suñol, J.J. Thermal analysis of Fe (Co, Ni) based alloys prepared by mechanical alloying. *J. Therm. Anal. Calorim.* **2007**, *87*, 255–258. [CrossRef]

9.   Bhobe, P.A.; Priolkar, K.R.; Nigam, A.K. Room temperature magnetocaloriceffect in Ni–Mn–In. *Appl. Phys. Lett.* **2007**, *91*, 242503. [CrossRef]

10. Sutou, Y.; Imano, Y.; Koeda, N.; Omori, T.; Kainuma, R.; Ishida, K.; Oikawa, K. Magnetic and martensitic transformations of NiMn$_X$ (X = In, Sn, Sb) ferromagnetic shape memory alloys. *Appl. Phys. Lett.* **2004**, *85*, 4358. [CrossRef]

11. Krenke, T.; Acet, M.; Wassermann, E.F.; Moya, X.; Manosa, L.; Planes, A. Martensitic transition and the nature of ferromagnetism in the austenitic and martensitic states of Ni-Mn-Sn alloys. *Phys. Rev. B* **2005**, *72*, 014412. [CrossRef]

12. Brown, P.J.; Gandy, A.P.; Ishida, K.; Kainuma, R.; Kanomata, T.; Neumann, K.U.; Ouladdiaf, B.; Ziebeck, K.R.A. The magnetic and structural properties of the magnetic shape memory compound Ni$_2$Mn$_{1.44}$Sn$_{0.56}$. *J. Phys. Condens. Matter* **2006**, *18*, 2249–2259. [CrossRef]

13. Koyama, K.; Watanabe, K.; Kanomata, T.; Kainuma, R.; Oikawa, K.; Ishida, K. Observation of field-induced reverse transformation in ferromagnetic shape memory alloy Ni$_{50}$Mn$_{36}$Sn$_{14}$. *Appl. Phys. Lett.* **2006**, *88*, 132505. [CrossRef]

14. Petrisek, V.; Dusek, M. *The Crystallographic Computing System*; Institute of Physics: Prague, Czech Republic, 2000; Available online: http://www.xrey.fzu.cz/jana/jana.html (accessed on 1 May 2020).

15. Coll, R.; Escoda, L.; Saurina, J.; Hernando, B.; Suñol, J.J. Martensitic transformation in Mn-Ni-Sn Heusler alloys. *J. Therm. Anal. Calorim.* **2010**, *99*, 905–909. [CrossRef]

16. Sánchez-Llamazares, J.L.; Sánchez, T.; Santos, J.-D.; Pérez, M.J.; Sánchez, M.L.; Hernando, B.; Escoda, L.; Suñol, J.J.; Varga, R. Martensitic phase transformation in rapidly solidified Mn$_{50}$Ni$_{40}$In$_{10}$ alloy ribbons. *Appl. Phys. Lett.* **2008**, *92*, 012513. [CrossRef]

17. Bachaga, T.; Daly, R.; Khitouni, M.; Escoda, L.; Saurina, J.; Suñol, J.J. Thermal and Structural Analysis of Mn$_{49.3}$Ni$_{43.7}$Sn$_{7.0}$ Heusler Alloy Ribbons. *J. Entropy* **2015**, *17*, 646–657. [CrossRef]

18. Rekik, H.; Krifa, M.; Bachaga, T.; Escoda, L.; Sunol, J.J.; Khitouni, M.; Chemingui, M. Structural and martensitic transformation of MnNiSn shape memory alloys. *Int. J. Adv. Manuf. Technol.* **2017**, *90*, 291–298. [CrossRef]

19. Zeng, H.; Wu, D.; Xue, S.; Frenzel, J.; Eggeler, G.; Zhai, Q. Martensitic transformation in rapidly solidified Heusler Ni$_{49}$Mn$_{39}$Sn$_{12}$ ribbons. *Acta Mater.* **2011**, *59*, 5692–5699. [CrossRef]

20. Kaufman, L.; Hullert, M. Thermodynamics of martensite transformation. In *Martensite*; Olson, G.B., Owen, W.S., Eds.; ASM International: Cambridge, UK, 1992; pp. 41–58.

21. Hernando, B.; Sanchez-Llamazares, J.L.; Santos, J.D.; Sanchez, M.L.; Escoda, L.; Sunol, J.J.; Varga, R.; Garcia, C.; Gonzalez, J. Grain oriented NiMnSn and NiMnIn Heusler alloys ribbons produced by melt spinning: Martensitic transformation and magnetic properties. *J. Magn. Magn. Mater.* **2009**, *321*, 763–768. [CrossRef]

22. Santos, J.D.; Sanchez, T.; Alvarez, P.; Sanchez, M.L.; Sanchez-Llamazares, J.L.; Hernando, B.; Escoda, L.; Suñol, J.J.; Varga, R. Microstructure and magnetic properties of Ni$_{50}$Mn$_{37}$Sn$_{13}$ Heusler alloy ribbons. *J. Appl. Phys.* **2008**, *103*, 07B326. [CrossRef]

23. Planes, A.; Manosa, L.; Acet, M. Magnetocaloric effect and its relation to shape-memory properties in ferromagnetic Heusler alloys. *J. Phys. Condens. Matter* **2009**, *21*, 233201. [CrossRef] [PubMed]

24. Sanchez-Alarcos, V.; Recarte, V.; Perez-Landazabal, J.L.; Gomez-Polo, C.; Rodriguez-Velamazan, J.A. Role of magnetism on the martensitic transformation in Ni–Mn-based magnetic shape memory alloys. *Acta Mater.* **2012**, *60*, 459–468. [CrossRef]

25. Chernenko, V.A. Compositional instability of beta-phase in Ni–Mn–Ga alloys. *Scr. Mater.* **1999**, *40*, 523–527. [CrossRef]

26. Krenke, T.; Moya, X.; Aksoy, S.; Acet, M.; Entel, P.; Manosa, L.; Planes, A.; Elerman, Y.; Yücel, A.; Wassermann, E.F. Electronic aspects of the martensitic transition in Ni–Mn based Heusler alloys. *J. Magn. Magn. Mater.* **2007**, *310*, 2788–2789. [CrossRef]

27. Deltell, A.; Escoda, L.; Saurina, J.; Suñol, J.J. Martensitic transformation in Ni-Mn-Sn-Co Heusler alloys. *Metals* **2015**, *5*, 695–705. [CrossRef]

28. Álvarez-Alonso, P.; Aguilar-Ortiz, C.O.; Villa, E.; Nespoli, A.; Flores-Zúñiga, H.; Chernenko, V.A. Conventional and inverse elastocaloric effect in Ni-Fe-Ga and Ni-Mn-Sn ribbons. *Scr. Mater.* **2017**, *128*, 36–40. [CrossRef]

29. Saini, D.; Singh, S.; Banerjee, M.K.; Sachdev, K. Microstructure and phase transformation in $Ni_{50}Mn_{40}Sn_{10}$ shape memory alloy. *Powder Metall. Met. Ceram.* **2018**, *57*, 361–366. [CrossRef]

30. Zhang, Y.; Billman, J.; Shamberger, P.J. Size effects in the martensitic transformation hysteresis in Ni-Mn-Sn Heusler alloy films. *Acta Mater.* **2019**, *180*, 116e125. [CrossRef]